

Radial-Velocity Curves and Theoretical Spectral-Line Profiles of the Components of Low-Mass Close X-ray Binary Systems

E. A. Antokhina¹, A. M. Cherepashchuk¹, and V. V. Shimanskii²

¹*Sternberg Astronomical Institute, Universitetskii pr. 13, Moscow, 119992 Russia*

²*Kazan State University, ul. Lenina 18, Kazan, 420008 Tatarstan, Russia*

Received March 30, 2004; in final form, July 15, 2004

Abstract—We present the results of calculations of theoretical absorption-line profiles and radial-velocity curves for optical components in X-ray binary systems. Tidal distortion of the optical star and X-ray heating by incident radiation from the relativistic object are taken into account. An emission component forms whose intensity varies with orbital phase in the absorption-line profile in the presence of significant X-ray heating. As a result, the width of the line decreases rather than increases at quadrature. The line profiles and equivalent widths and the radial-velocity curves depend substantially on the parameters of the binary systems. This provides the possibility of directly determining component masses and orbital inclinations from high-resolution spectroscopic observations of X-ray binary systems. © 2005 Pleiades Publishing, Inc.

1. INTRODUCTION

Antokhina and Cherepashchuk [1] and Shahbaz [2] suggested a new method to estimate the component-mass ratios q and orbital inclinations i of X-ray binary systems using data on the orbital variability of absorption-line profiles in the spectrum of the optical component. This variability is due to the finite size of the optical star, tidal distortion by the companion, and the complex pattern of its surface-temperature distribution. In point-source or spherical models for binary components, the line profile and, accordingly, the shape of the radial-velocity curve, does not depend on the orbital inclination i . For this reason, radial-velocity curves can yield only the product $m \sin^3 i$ (where m is mass of the star). If a star with a significant size is tidally distorted, the shape of the line profiles and radial-velocity curve depend on i and q . In principle, this provides the possibility of deriving both the component masses and the orbital inclination from the orbital variations of line profiles (or from the corresponding radial-velocity curve). Recently, Abubekkerov *et al.* [3] used this approach to estimate the mass of the black-hole component of the X-ray binary Cyg X-1 and the orbital inclination of the system based on a high-precision radial-velocity curve.

In our earlier work [1, 4, 5], we calculated line profiles for tidally-distorted components of binary systems using theoretical hydrogen-line profiles for various effective temperatures T_{eff} and surface gravities g computed by Kurucz [6]. The reflection effect was taken into account using a model implementing a simple summation of the radiated and incident fluxes,

without considering the transfer of the incident radiation in the atmosphere of the externally heated star. This approach is not completely correct; in particular, it does not enable us to take into account emission components of the lines that may arise in the case of strong heating by incident radiation. For X-ray binaries, such a crude model is valid only in the case of weak X-ray heating, when the ratio of the bolometric luminosities of the X-ray source (L_x) and optical star (L_v) is $k_x = L_x/L_v < 1$.

In the present study, we have computed absorption-line profiles for a tidally-distorted optical star in an X-ray system by correctly solving for the radiative transfer in the line at a given point of the stellar surface in the presence of external X-ray irradiation.

2. MODEL OF THE BINARY SYSTEM

The basic idea behind the synthesis of theoretical light curves and stellar spectral-line profiles is the decomposition of the complex stellar surfaces into thousands of area elements for which the outgoing local flux is computed. The contributions of the areas are summed for each orbital phase, taking into account the Doppler effects and visibilities of the areas. Thus, for each orbital phase, we can find the radiation flux in the continuum directed toward the observer and the rotationally broadened spectral line profiles, which enables us to determine the radial velocity of the star. Line synthesis is able to allow for effects related to the proximity of the components in a binary system: tidal–rotational distortion of the stars (the ellipticity effect), the nonuniform temperature distribution over the stellar surface due to gravitational

darkening, heating due to irradiation by a companion (the reflection effect), and other effects.

The first version of our line-synthesis algorithm for X-ray binaries with circular orbits was described in [7]. Here, we present a new algorithm for the computation of theoretical line profiles and the construction of radial-velocity curves. The line profiles of area elements on the surface of a star are computed using models in which their atmospheres are subject to incident X-ray radiation. This new algorithm for computing theoretical spectral-line profiles opens broad possibilities for more correct interpretations of spectroscopic observations and the derivation of reliable physical parameters of close binaries. It also makes it possible to derive theoretical line profiles for stars that are subject to ultraviolet or optical irradiation.

We consider here an X-ray binary system. Let us describe the main features of our algorithm for modeling theoretical line profiles for the optical star in the binary and the construction of the binary's radial-velocity curve. The binary consists of an optical star and a relativistic object, which usually move in elliptic orbits about their center of mass. The orbital inclination is i and the component-mass ratio is $q = M_x/M_v$, where M_x is the mass of the relativistic object and M_v the mass of the optical star. The surface of the star coincides with the Roche equipotential surface, and the size of the star is determined by the Roche-lobe filling factor μ_v , where $\mu_v = R/R^*$ is the ratio of the polar radii for partial and total Roche-lobe filling. The star's rotation can be asynchronous with the orbital motion [5], with the degree of asynchronous rotation specified by the parameter $F = \omega_{rot}/\omega_K$, where ω_{rot} is the angular velocity of the rotation, ω_K is the mean Keplerian orbital angular velocity ($\omega_K = 2\pi/P$), and P the orbital period of the binary.

We introduce a Cartesian coordinate system (X, Y, Z) with its origin at the center of mass of the optical star. The X axis is directed along the line passing through the component centers, the Y axis lies in the orbital plane, and the Z axis is perpendicular to the orbital plane. We also introduce a spherical coordinate system (r, η, ψ) with its origin at the center of the optical star. The stellar surface is decomposed into a large number of area elements. Let \mathbf{r} be the radius vector of a surface element, and λ, ν the direction cosines of \mathbf{r} relative to the X, Z axes (see [5] for more details). In the spherical coordinate system (r, η, ψ) , the equation for the equipotential surface of the star is [8]

$$\Omega = \frac{1}{r} + q \left(\frac{1}{\sqrt{D^2 + r^2 - 2Dr\lambda}} - \frac{r\lambda}{D^2} \right) + \frac{1}{2}(1+q)r^2F^2(1-\nu^2). \quad (1)$$

Here, D is the instantaneous distance between the centers of the stars moving in elliptical orbits and r is measured in units of D .

The equation for the equipotential surface is solved numerically for every surface element for fixed η, ψ , and the radius vector \mathbf{r} and coordinates x, y, z are found. The local surface gravity $g(\mathbf{r}) = |\text{grad}\Omega|$ is also computed for every surface element (in relative units; it is converted into absolute units later), as well as the coordinates of the unit normal vector

$$\mathbf{n} = -\frac{\text{grad}\Omega}{|\text{grad}\Omega|}. \quad (2)$$

In the first stage of the computations, the temperature of a surface element is found, taking into account only gravitational darkening. The effect of the incident radiation is taken into account later, when the model atmosphere is computed for every element:

$$T(\mathbf{r}) = T_0 \left(\frac{g(\mathbf{r})}{g_0} \right)^\beta, \quad (3)$$

where T_0 is the mean effective temperature of the star, $g(\mathbf{r})$ and g_0 are the local gravity and the effective gravity averaged over the stellar surface, and β is the gravitational-darkening coefficient. For a star in radiative equilibrium, $\beta = 0.25$ [9], while $\beta = 0.08$ for a star with a convective envelope [10].

We can compute for each surface element the parameter K_x^{loc} : the ratio of the incident X-ray flux H and the total flux radiated by the corresponding non-irradiated atmosphere H_0 :

$$K_x^{loc} = \frac{H}{H_0} = \frac{k_x L_v \cos \theta}{4\pi\rho^2\sigma T^4(\mathbf{r})}. \quad (4)$$

Here, k_x is the ratio of the X-ray luminosity of the compact object and the bolometric luminosity of the star, L_v is the bolometric luminosity of the optical star, σ is the Stefan–Boltzmann constant, $T(\mathbf{r})$ is the effective temperature of the surface element, θ is the angle between the normal to the surface and the direction to the X-ray source, and ρ is the distance from the center of the surface element to the X-ray source. For surfaces that are not subject to incident radiation, $K_x^{loc} = 0$. The value of K_x^{loc} is an input parameter for the routine that computes the local model atmosphere for a surface element; this procedure will be described in the next section.

To compute the stellar emission at various orbital phases, we introduce a stationary Cartesian coordinate system $(\bar{X}, \bar{Y}, \bar{Z})$ with its origin at the star's center of mass. The relative rotation angle of the components θ_{orb} is the angle between the X and \bar{X} axes. At orbital phase $\varphi = 0$, the first star eclipses the secondary and $\theta_{orb} = 0^\circ$. The coordinates of a unit

vector pointing in the direction of the observer in the moving (X, Y, Z) coordinate system are

$$\mathbf{a}_0 = (-\sin i \cos \theta_{orb}, -\sin i \sin \theta_{orb}, \cos i) \quad (5)$$

$$= (a_x, a_y, a_z).$$

The cosine of the angle γ between the normal to the surface element and the direction to the observer is then defined as the scalar product $\cos \gamma = (\mathbf{a}_0, \mathbf{n})$. If $\cos \gamma > 0$, a surface element can be seen by the observer. The total observed emission of the star is obtained by summing the fluxes from all observable surface elements in the direction toward the observer at each orbital phase.

Let consider the procedure for computing the velocities of the surface elements relative to the star's center of mass. Let us take a surface element with its center at the coordinates (x, y, z) . The velocity of the element \mathbf{v} relative to the center of mass in the stationary coordinate system (X, Y, Z) is

$$\mathbf{v} = [\boldsymbol{\omega}_{rot}, \mathbf{r}] = (\omega_{rot}y, -\omega_{rot}x, 0). \quad (6)$$

Here, $\boldsymbol{\omega}_{rot}$ is the angular velocity of the stellar rotation, $\boldsymbol{\omega}_{rot} = (0, 0, \omega_z = \omega_{rot} = \omega)$. The projection of \mathbf{v} onto the line of sight directed away from the observer (when the velocity is positive away from the observer) is

$$v_r = (-\mathbf{v} \cdot \mathbf{a}) = (\omega_{rot}y, -\omega_{rot}x, 0) \quad (7)$$

$$\times (-a_x, -a_y, -a_z) = -\omega_{rot}y a_x + \omega_{rot}x a_y.$$

Let the radial velocity of the center of mass of the star be V_c . The resultant velocity of the surface element relative to the center of mass of the system (projected onto the line of sight) is then

$$V_r = v_r + V_c. \quad (8)$$

Thus, it is possible to compute the radial velocities of all the surface elements over the star for every orbital phase. The summation of the local spectral-line profiles and computation of the total line profile for a star at different orbital phases is done taking into account the Doppler shifts of the local profiles relative to the velocity of the center of mass of the star.

Let us now describe the procedure for computing the local absorption-line profile of a surface element with effective temperature T , local effective gravity g , and irradiation parameter K_x^{loc} , which is the ratio of the incident X-ray flux to the emitted flux (in the absence of irradiation).

3. COMPUTATION OF THE MODEL ATMOSPHERE AND THE EMISSION SPECTRUM FOR A SURFACE ELEMENT

To correctly compute the continuum emission and line profiles of the local surface elements, it is necessary to make a preliminary estimate of the structure

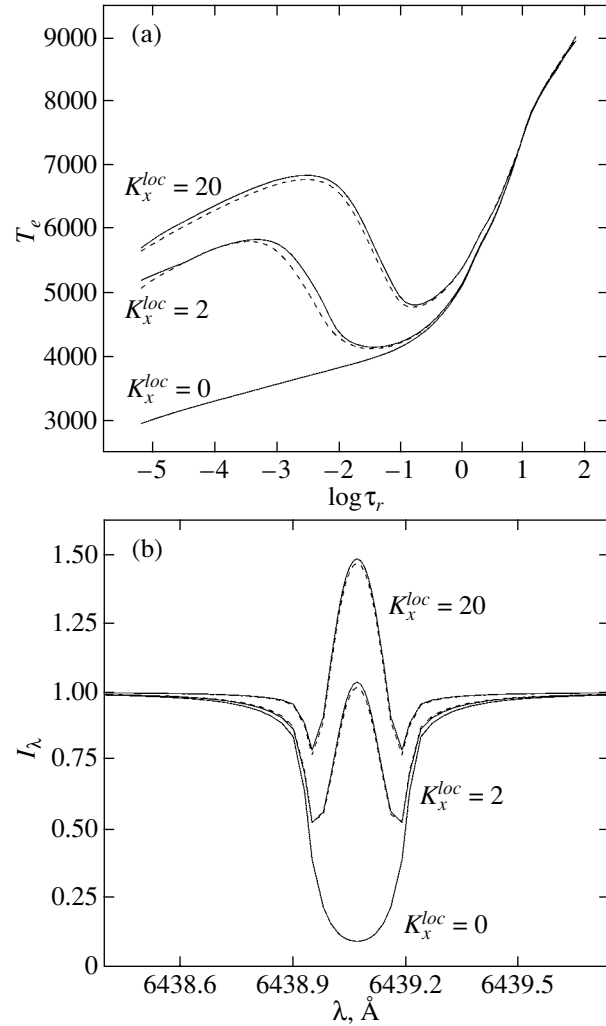


Fig. 1. (a) Comparison of the distributions of the electron temperature T_e in models computed using the method of heating- and cooling-function balance (dashed) and in precise blanketed models with atmospheric parameters $T_{eff} = 4752$ K, $\log g = 2.63$ and various irradiation coefficients K_x^{loc} (solid). (b) Comparison of the CaI $\lambda 6439.075$ Å line profiles computed for the atmospheres shown in (a).

of the stellar atmosphere in the presence or absence of irradiation. In general, this requires that we solve the radiative-transfer equations

$$\mu \frac{dI_\nu}{dr} = \alpha_\nu (S_\nu - I_\nu) \quad (9)$$

for a set of frequencies ν , some of which are present in the incident flux, which has angle of incidence θ ($\mu = \cos \theta$) and power μI_ν^+ .

The standard conditions of radiative and hydro-

static stability are fulfilled for each atmospheric layer: or

$$\int_0^{\infty} \int_{-1}^1 \alpha_{\nu} I_{\nu} d\mu d\nu = \int_0^{\infty} \int_{-1}^1 \alpha_{\nu} S_{\nu} d\mu d\nu, \quad (10)$$

$$\frac{dp}{dm} = g, \quad (11)$$

where m is the mass of a unit column of gas measured down from the upper boundary. The solution of this problem using standard software packages developed for nonirradiated atmospheres (e.g., ATLAS 9 [11]) encounters considerable difficulties, due to the dependence of the incident radiation on the angle θ , which is close to a δ function. This contradicts the basic assumption that the radiation intensity depends smoothly on μ , which is applied in subroutines for the numerical solution of the radiative-transfer equation in ATLAS-type software packages.

For this reason, we suggest a different approach to computing the atmospheric structure, which takes into account the lack of any direct interaction between the incident radiation and the intrinsic stellar radiation. In the first step of this procedure, the set of equations (9) is solved with a nonzero upper boundary condition, specified values of μ , and a source function S_{ν} that is equal to zero. This yields the dependences of the distributions of the mean intensity J_{ν} and the flux H_{ν} on the optical depth τ_{ν} at the frequency ν in the form

$$J_{\nu}^{+}(\tau_{\nu}) = I_{\nu}^{+} \exp(-\tau_{\nu}/\mu), \quad (12)$$

$$H_{\nu}^{+}(\tau_{\nu}) = \mu I_{\nu}^{+} \exp(-\tau_{\nu}/\mu). \quad (13)$$

In the second step, Eqs. (9) are solved again, but with a zero upper boundary condition, a set of μ values, and a source function determined by the sum of the total scattered (including external) radiation and the Planck function for each layer:

$$S_{\nu} = \frac{2\alpha'_{\nu} B_{\nu}(\tau_{\nu}) + \sigma_e \int_{-1}^1 I_{\nu} d\mu}{2(\alpha'_{\nu} + \sigma_e)}, \quad (14)$$

where α'_{ν} and σ_e are the true-absorption and electron-scattering coefficients.

A simple expression for the distribution of the source function over optical depth is given in [12], where this problem is solved for a gray model with mean opacity coefficients for the external and intrinsic radiation α_x and α_v :

$$S(\tau_v) = S^0(\tau_v) + I^+ \frac{\alpha_x}{\alpha_v} \exp\left(-\frac{\alpha_x \tau_v}{\alpha_v \mu}\right) + \frac{1}{2} \mu I^+ + \frac{3\mu \alpha_v}{4\alpha_x} \mu I^+ \left[1 - \exp\left(-\frac{\alpha_x \tau_v}{\alpha_v \mu}\right)\right] \quad (15)$$

$$S(\tau_v) = S^0(\tau_v) + a_2 S_2(\tau_v) + a_3 S_3(\tau_v) + a_4 S_4(\tau_v), \quad (16)$$

where $S^0(\tau_v) = \sigma T_e^4$ is the distribution for a non-irradiated atmosphere.

The presence in Eq. (15) of the term $S_2(\tau_v)$, which decreases exponentially with depth, results in a negative gradient $dS(\tau_v)/d\tau_v$ in the upper layers of the stellar atmosphere; i.e., in the formation of a high-temperature chromosphere. Equation (15) shows that the source-function excess in the chromosphere is proportional to the ratio α_x/α_v . As was shown in [12], the absorption coefficient of stellar material with T_e below 100 000 K in the X-ray range depends on ν as a power-law with an exponent close to -2.3 . Therefore, the presence in the incident flux of even a weak soft component with $E < 2.0$ keV (with $\alpha_x/\alpha_v \gg 1$) results in the rapid growth of the temperature in the chromospheric layers and the development of strong emission features in the emitted stellar spectra. This circumstance demands a rigorous determination of the frequency distribution in the incident flux in the course of the modeling (see also [13]).

Subsequent computations of exact blanketed model atmospheres with irradiation [14] have shown that their temperature structure is described well by Eq. (16). In this case, the terms S_2 , S_3 , and S_4 must be written in quadrature form:

$$S_2(\tau_v) = \int_{\nu_1}^{\nu_2} \frac{dH_{\nu}^{+}(\tau_v)}{d\tau_v} d\nu_x, \quad (17)$$

$$S_3(\tau_v) = \int_{\nu_1}^{\nu_2} H_{\nu}^{+}(\tau'_v = 1) d\nu_x, \quad (18)$$

$$S_4(\tau_v) = \int_{\nu_1}^{\nu_2} \int_0^{\tau_v} \left(S_2(\tau'_v) + H_{\nu}^{+}(\tau'_v)\right) d\tau'_v d\nu_x. \quad (19)$$

They are easily found numerically for a given frequency distribution for the incident flux H_{ν}^{+} , incidence angle θ , and ratio of the absorption coefficients at the frequencies of the external and intrinsic radiation $\alpha_x(\tau_v)/\alpha_v(\tau_v)$, which is found in the course of the computations. In our method, the absorption coefficient α_x at the frequencies of the incident radiation is computed allowing for ionization from the inner and outer shells of hydrogen, helium, and the 20 most abundant heavy elements in five ionization stages in accordance with Yakovlev *et al.* [15], and also including Thompson scattering. As was shown by Sakhbullin and Shimanskii [14], the absorption

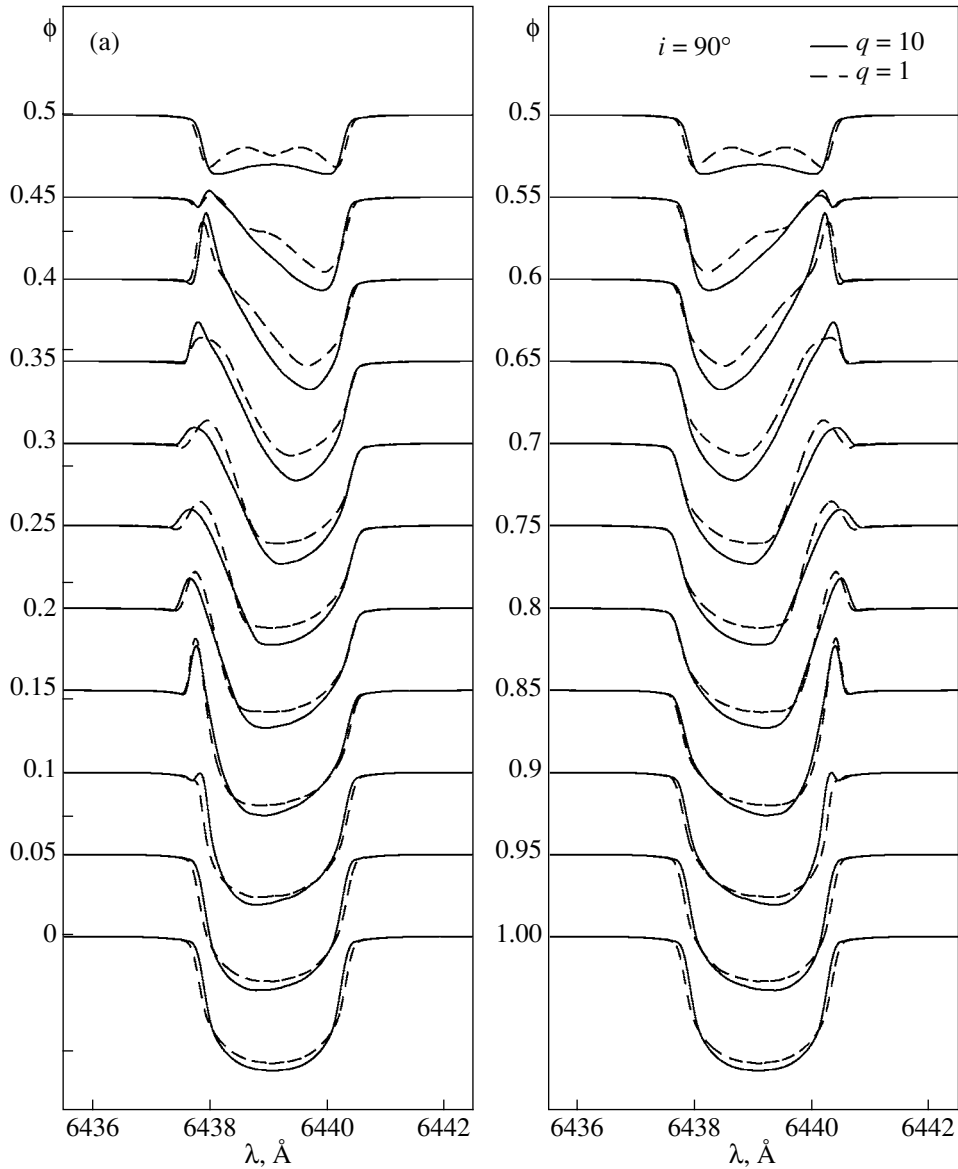


Fig. 2. Orbital-phase variations of the Ca I $\lambda 6439$ Å line profile in the spectrum of an X-ray-irradiated star ($k_x = 10$) for the two orbital inclinations (a) $i = 90^\circ$ and (b) $i = 45^\circ$. The profiles are normalized to the continuum, and Doppler shifts have been subtracted. At phase $\phi = 0$, the optical star is in front of the X-ray source. The parameters of the optical star are $M_v = 1M_\odot$, $\mu_v = 1$, and $T = 5000$ K. Line profiles are shown for the two component-mass ratios $q = 10$, $M_x = 10M_\odot$ (solid) and $q = 1$, $M_x = 1M_\odot$ (dashed).

coefficient at the frequencies of the intrinsic atmospheric radiation α_v can be represented with high accuracy by combinations of Planck and Rosseland absorption coefficients, α_p and α_r . Fitting our models of irradiated atmospheres obtained using this method and of exact blanketed models obtained using the BINARY 3 code [14] yielded the following expression for α_v [16]:

$$\alpha_v = (\alpha_r^{5.97+0.73 \log \tau_r} \alpha_p)^{\frac{1}{6.97+0.73 \log \tau_r}}. \quad (20)$$

Simultaneously, the weight coefficients for the

components of the complete source function (16) were found: $a_2 = 0.67$, $a_3 = 0.51$, and $a_4 = 0.63$. Our method for modeling the atmospheres of irradiated stars has certain advantages when applied to binary stars.

(1) The determination of the temperature structure of the irradiated atmosphere is based on the balance of the gas heating and cooling functions, but not on the standard methods of temperature correction. As is noted in [14], the temperature correction diverges for models of irradiated atmospheres if the flux gradients

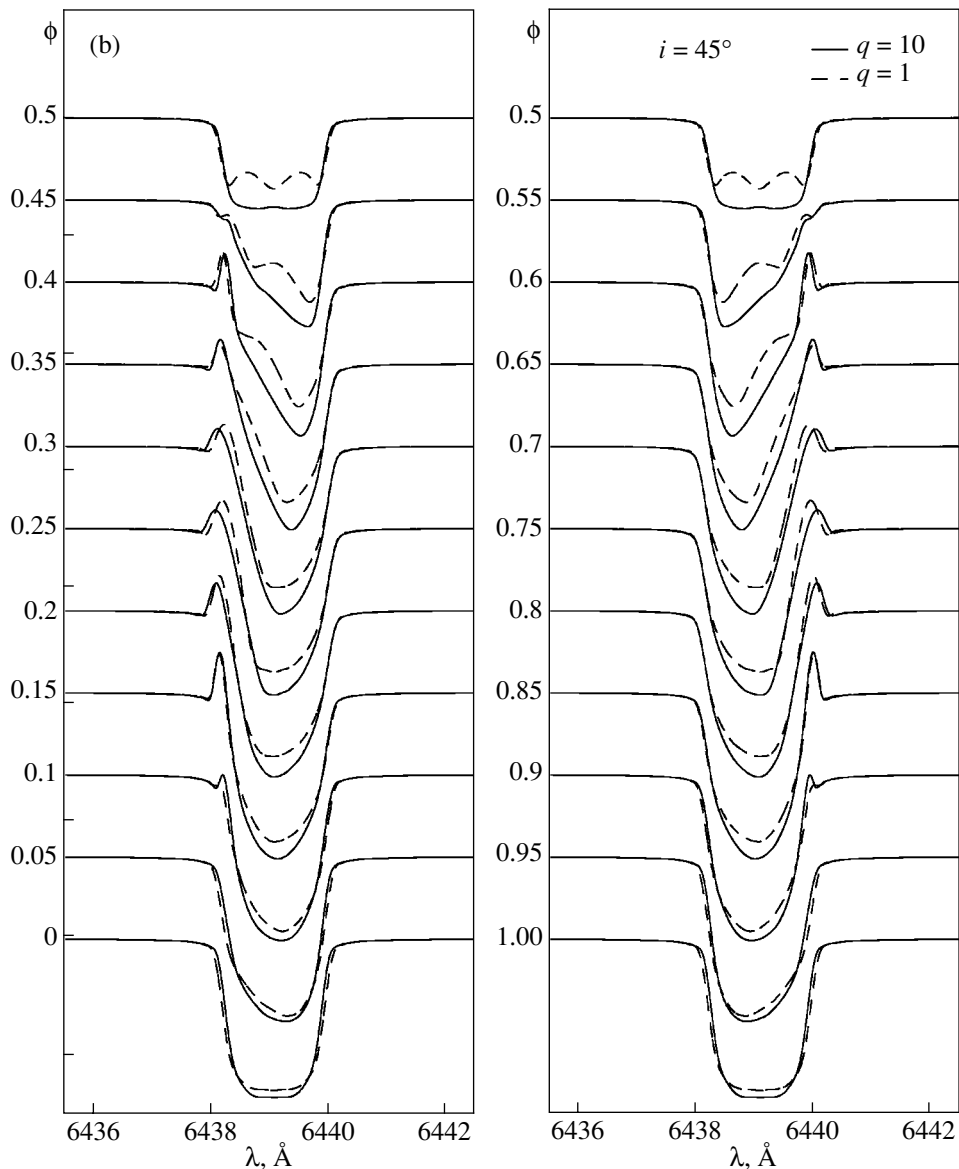


Fig. 2. (Contd.)

in high layers are large. Therefore, as a rule, correction methods cannot be used to compute model atmospheres with strong irradiation. At the same time, the method of heating- and cooling-function balance remains stable even for irradiation coefficients K_x^{loc} in the hundreds. Moreover, since it is not necessary to solve the radiation-transfer equation for optical frequencies, the required computational time decreases by a factor of 30–80, which is especially important for close binary systems.

(2) The source function of the irradiated atmosphere $S(\tau_\nu)$ is determined by the change of the initial source function of an ordinary atmosphere $S^0(\tau_\nu)$, when the terms S_2 , S_3 , and S_4 , which depend linearly

on H_ν^+ , appear. As a result, the temperature structure characteristic of a nonirradiated atmosphere is preserved in the case of small or zero incident fluxes. This makes it possible to use our method to study binary stars and single stars with weak reflection effects. Note that the initial models for the nonirradiated atmospheres were found by interpolating the grids of Kurucz [11] for blanketed models for specified T_{eff} and $\log g$ values, as is described in [17].

(3) Our method is able to compute models of stellar atmospheres irradiated by X-ray, UV, and optical radiation with an accuracy sufficient for numerical studies of close binary stars. It was shown in [16] that the errors in the temperature distribution do not exceed 4% for model atmospheres with incident fluxes

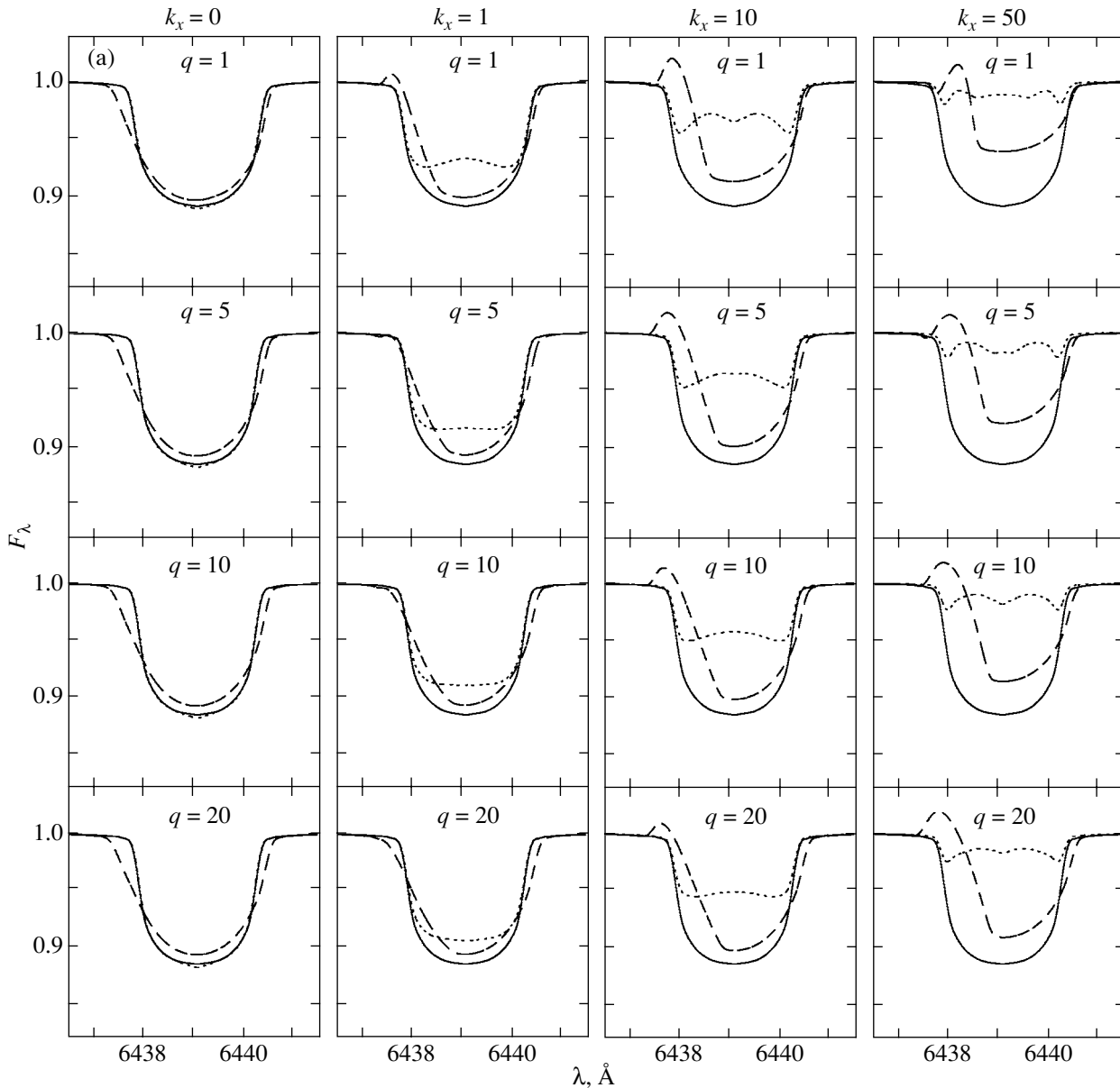


Fig. 3. Dependence of the Ca I $\lambda 6439$ Å line profiles on q and k_x for the two orbital inclinations (a) $i = 90^\circ$ and (b) $i = 45^\circ$. The model parameters cover the ranges $q = 1-20$, $k_x = 0-50$, $\mu_v = 1$, and $T = 5000$ K, $i = 90^\circ$. The profiles are shown for the three orbital phases $\varphi = 0$, when the X-ray source is behind the optical star (solid), $\varphi = 0.25$, when the star is viewed from the side (dashed), and $\varphi = 0.5$, when the X-ray source is in front of the optical star (dotted).

with $K_x^{loc} < 100$ and for wavelengths $0.30 \text{ \AA} \leq \lambda \leq 50.0 \text{ \AA}$, $250 \text{ \AA} \leq \lambda \leq 3000 \text{ \AA}$. The corresponding errors in the total radiated fluxes in the regions of the Balmer and Paschen continua are 1–3%.

We compared model atmospheres computed using the above method and blanketed models computed using the BINARY 3 code [14]. Figure 1 shows the results for two sets of input atmospheric parameters for the models in which we are directly interested: $T_{eff} = 4752$ K, $\log g = 2.63$, and $K_x^{loc} = 2.0$ and 20.0. Figure 1a shows the temperature dis-

tributions in the irradiated and nonirradiated atmospheres, while Fig. 1b shows the corresponding Ca I $\lambda 6439.075$ Å line profiles. This comparison shows that the maximum errors in T_e are less than 4% and are larger in the model with weaker irradiation ($K_x^{loc} = 2.0$), in particular, in the narrow transition region from the chromospheric layers to the temperature minimum. The difference in the Ca I line profiles that arise when the two different computational methods are applied results in variations of the equivalent widths that are less than $\Delta W_\lambda = 8 \text{ m\AA}$. Thus, we

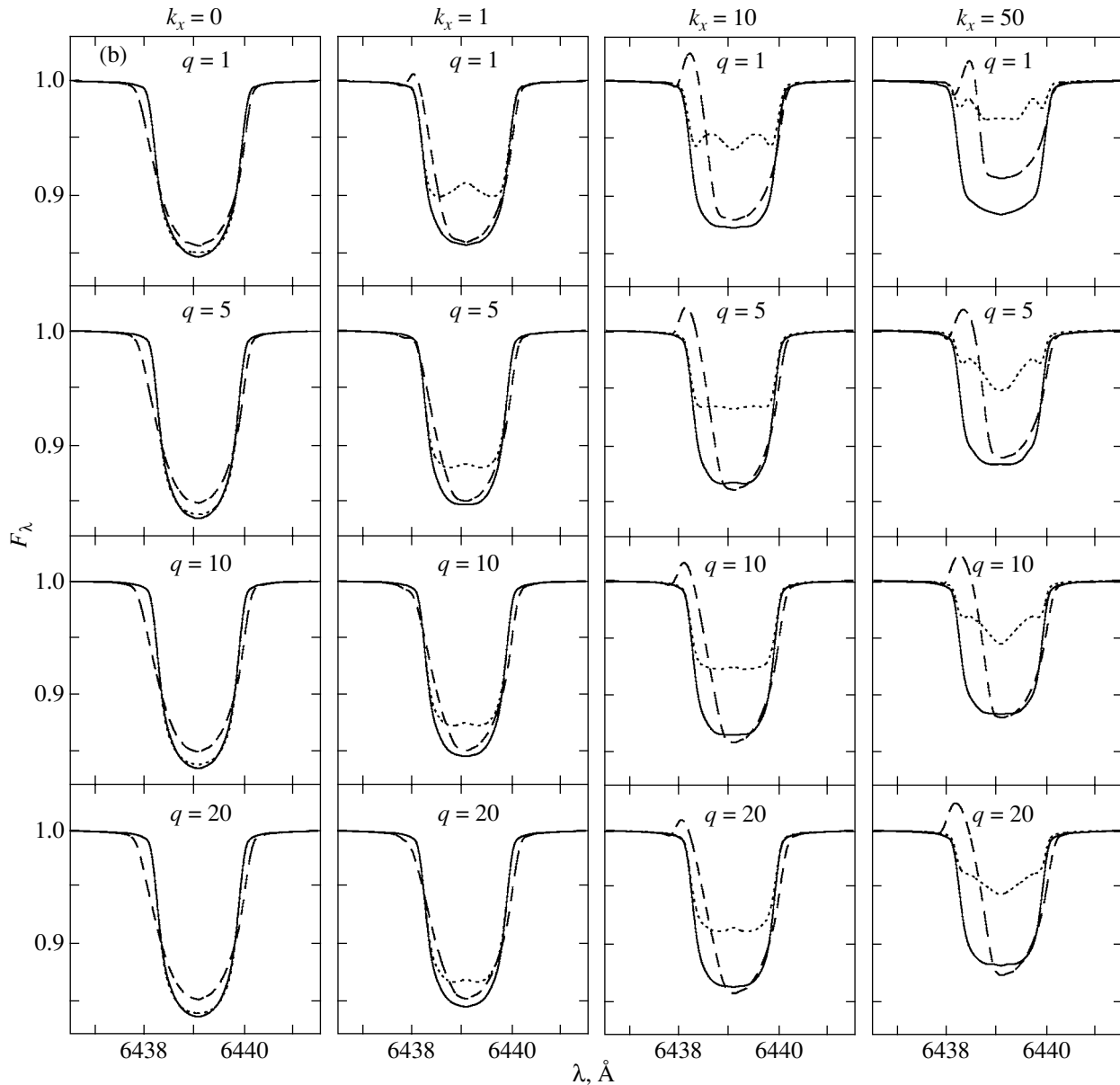


Fig. 3. (Contd.)

conclude that our method is fully adequate for the modeling of irradiated atmospheres.

The specific intensity of the radiation in the computed model atmospheres was found at three main angles θ' (for $\cos \theta' = 0.11, 0.50, 0.89$) by solving the radiative-transfer equation using the Hermitian method. The emission in the direction of the observer was subsequently computed by interpolating between the intensities for the three angles θ' for the real surface-element viewing angle γ . In this way, we physically accurately determined the emitted fluxes taking into account limb darkening using the model atmospheres.

The solution of the radiative-transfer equation included all sources of continuum absorption tabulated in the ATLAS 5 [18], STARDISK [19], and SPECTR [20] software packages, as well as the strongest lines and main molecular bands, according to the theoretical analysis of Nersisyan *et al.* [21]; the line and molecular-band data were derived and kindly provided to us by Ya. Pavlenko (Main Astronomical Observatory of the National Academy of Sciences of Ukraine). When computing the Balmer lines of H I, we applied the theory of Griem [22]; the oscillator strengths for He I lines were taken from [23, 24], and the corresponding broadening parameters were found using the approximation of Barnard *et al.* [25] and

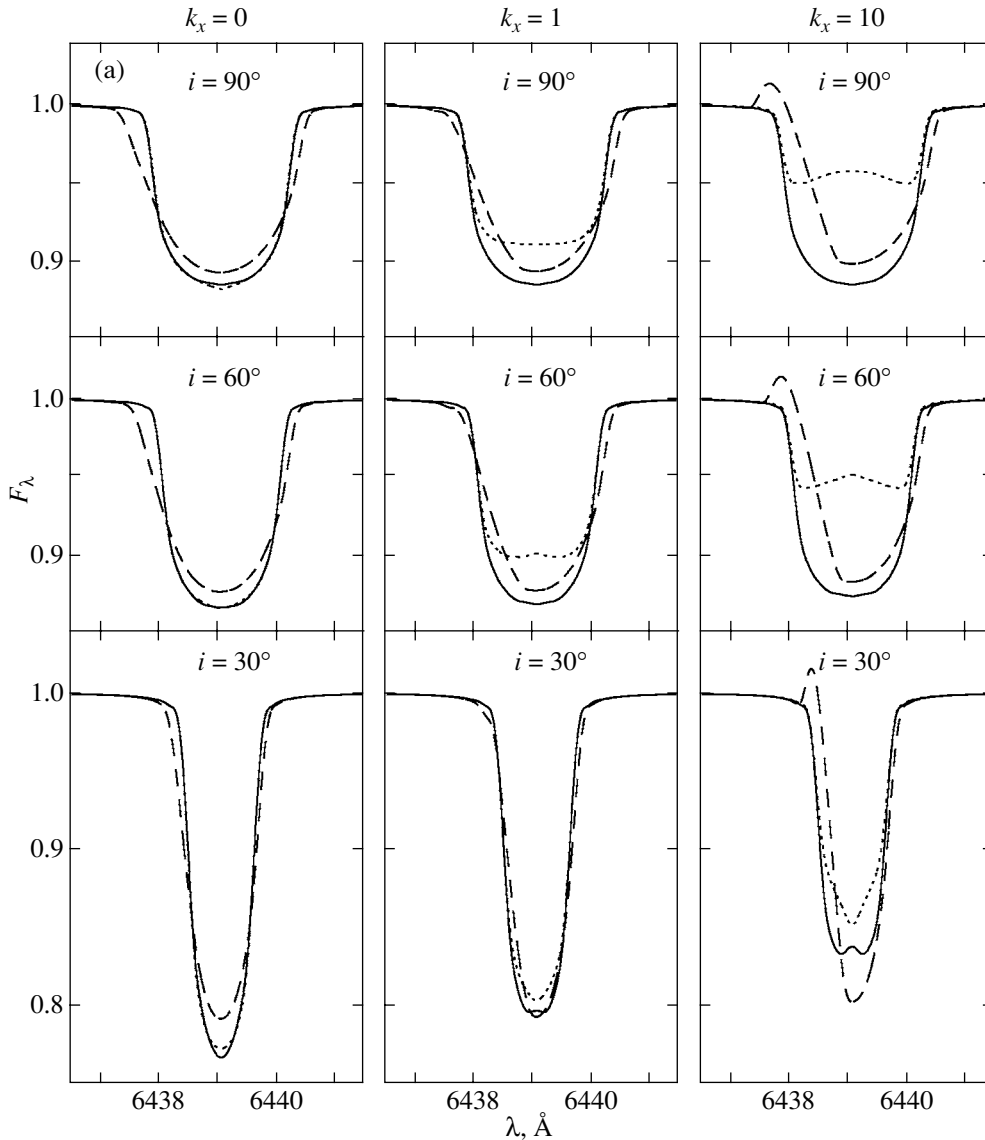


Fig. 4. Dependence of the CaI $\lambda 6439$ Å line profile on i and k_x for the two orbital inclinations (a) $i = 90^\circ$ and (b) $i = 45^\circ$. The model parameters are $i = 30^\circ - 90^\circ$, $k_x = 0 - 10$, $q = 10$, $\mu_v = 1$, and $T = 5000$ K. Profiles are shown for orbital phases $\varphi = 0$ (solid), 0.25 (dashed), and 0.5 (dotted).

Mihalas *et al.* [26]. The oscillator strengths for lines of heavy elements were taken from Kurucz [11], the van der Waals broadening constants C_6 were found using the classical formula of Unsold [27] with the scaling factor $\Delta \log C_6 = 0.7$, and the Stark broadening constants C_4 were found using the approximation of Kurucz and Furenlid [28]. All the line-profile computations took into account Doppler broadening due to thermal motions and microturbulence (which was assumed constant with $\xi_{turb} = 1.5$ km/s), as well as natural damping, and assumed the solar chemical abundance given in [29].

4. MODELING OF THE THEORETICAL SPECTRAL-LINE PROFILES FOR THE OPTICAL STAR IN AN X-RAY SYSTEM

Let us list the main input parameters for the synthesis of theoretical line profiles for a close binary system containing an optical star and a pointlike compact object that is a source of X-ray emission. The masses of the optical star M_v and X-ray source M_x and the orbital period are given in absolute units. The other input parameters are the Roche-lobe filling factor μ_v , mean effective temperature of the star T (without allowance for heating), ratio of the X-ray luminosity of the compact object and the bolomet-

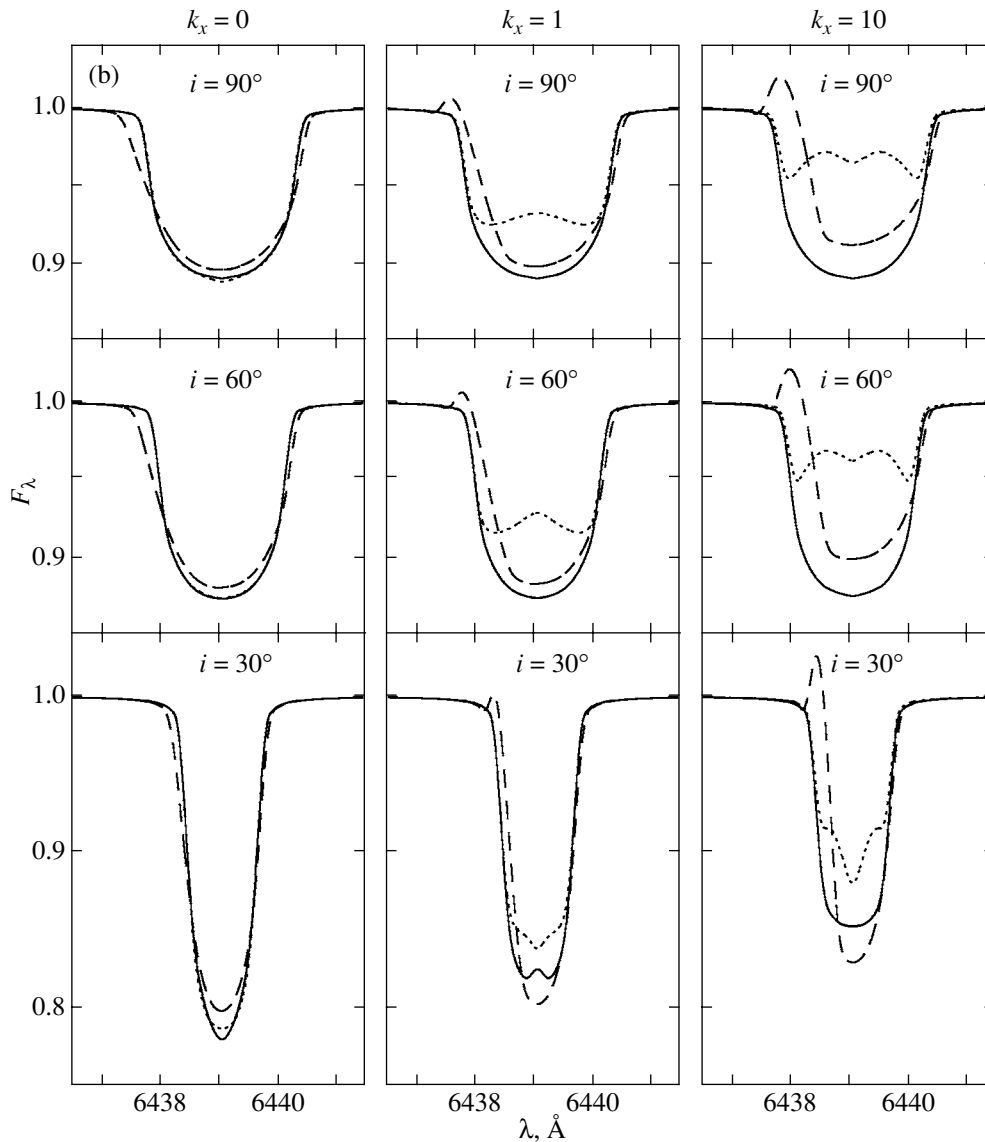


Fig. 4. (Contd.)

ric luminosity of the normal star k_x , gravitational-darkening coefficient β , orbital inclination i , orbital eccentricity e , longitude of periastron ω , and degree of asynchronous rotation F . The data on spectral lines and the spectrum of the compact object are also used as input data.

We selected input parameters that were close to the parameters of low-mass X-ray novae to model the theoretical line profiles. The mass $M_v = 1M_\odot$ and temperature $T = 5000$ K of the optical star were kept fixed. The gravitational-darkening coefficient was assigned the value $\beta = 0.08$ (standard for stars with convective envelopes). The stellar rotation was assumed to be synchronous with the orbital revolution ($F = 1$), and the orbit to be circular. The orbital period was taken to be $P = 5^d$ ($P = 12^d$ for the computation

of the radial-velocity curves). The spectrum of the external compact object in the wavelength range 12–0.5 Å (photon energies of 1–20 keV) was given by the function

$$I_x(\nu) = I_x \nu^{-0.6}. \quad (21)$$

We studied the behavior of the line profiles of the optical star during the orbital motion for various powers of the incident X-ray flux k_x . The component-mass ratio $q = M_x/M_v$, Roche-lobe filling factor μ_v , and orbital inclination i were varied as well. Theoretical profiles were computed for the CaI $\lambda 6439.075$ Å absorption line. We did not include non-LTE effects when modeling this line for a star with $T = 5000$ K. In their recent study of the formation of lines of heavy elements in the spectra of X-ray-irradiated cool stars,

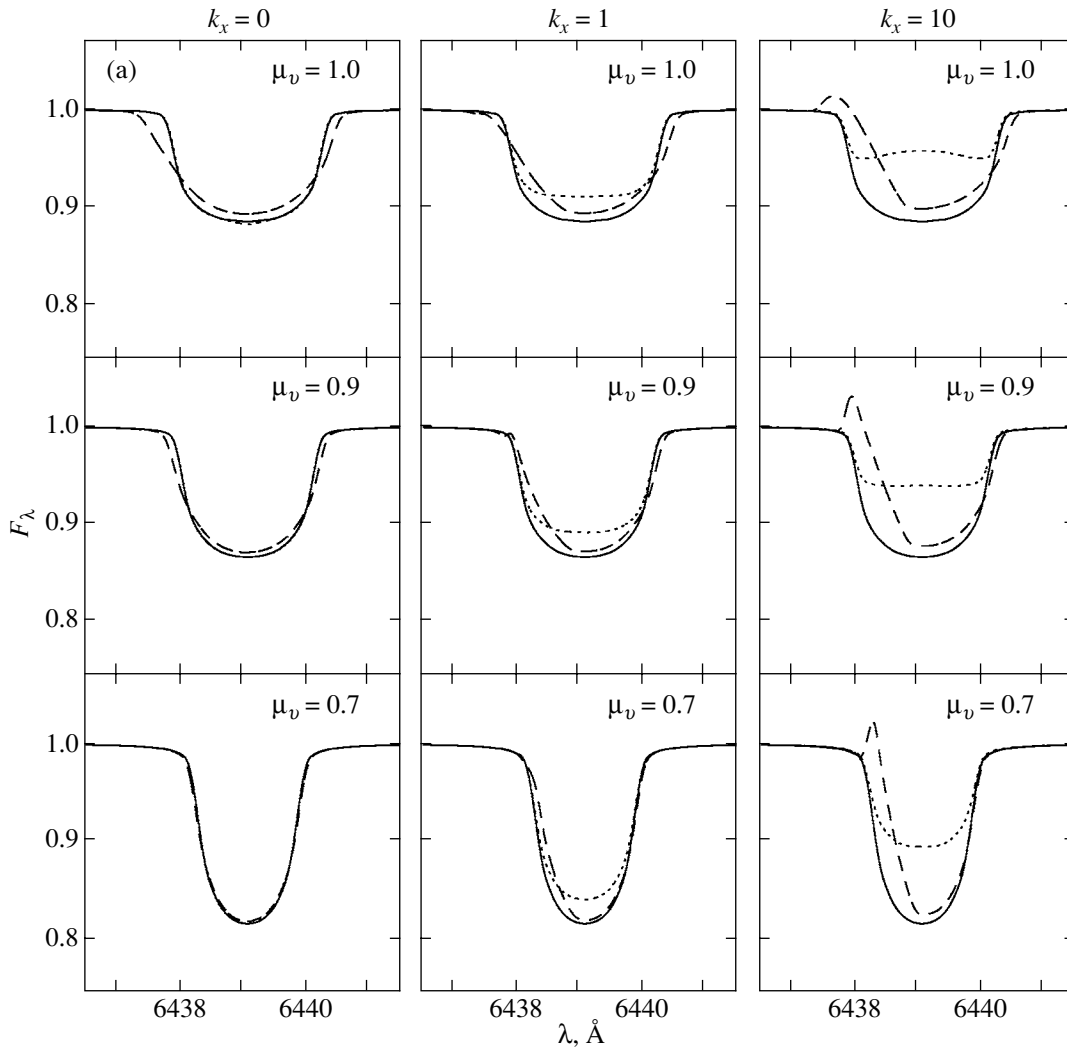


Fig. 5. Dependence of the CaI $\lambda 6439$ Å line profiles on μ_v and k_x for the two orbital inclinations (a) $i = 90^\circ$ and (b) $i = 45^\circ$. The model parameters are $\mu_v = 0.7-1.0$, $k_x = 0-10$, and $q = 10$. Profiles are shown for orbital phases $\varphi = 0$ (solid), 0.25 (dashed), and 0.5 (dotted).

Sakhbullin and Shimanskii [30] showed that non-LTE effects do appear in the atmospheres of such cool stars, but, although the numerical parameters change by 10–20%, the results obtained assuming LTE remain qualitatively correct.

Figure 2 shows the variations of the shape and intensity of the line profile with orbital phase for $k_x = 10$ and $i = 45^\circ$ and 90° using a dense grid in phase. We can clearly see the evolution of the summed line profile of the optical star as it turns the X-ray-heated side toward the observer. At phase 0, the optical star is in front of the X-ray source, and the unheated portion of the surface of the optical star is observed. Starting from about $\varphi = 0.1$, we begin to see the part of the star that is heated by external radiation. At $\varphi = 0.25$ (quadrature), the size of the star in the frontal plane is maximum, and both unheated and

heated parts of the star are observed. At phase 0.5, the part of the star that is maximally heated by the incident X-ray radiation is fully turned toward the observer. As the phase increases from 0 to 0.5, an emission component of the profile forms in the region of the star heated by the incident radiation, becoming increasingly prominent in the summed line profile. After phase 0.5, the contribution of the emission feature begins to diminish. The line profiles are symmetric about phase $\varphi = 0.5$. At orbital phases when both heated and unheated regions of the star moving with different velocities can be observed, the absorption profile becomes narrower due to the formation of the emission component.

We emphasize that, in the case of a pure ellipticity effect for an optical star without X-ray heating, the width of the line increases at quadrature, when the

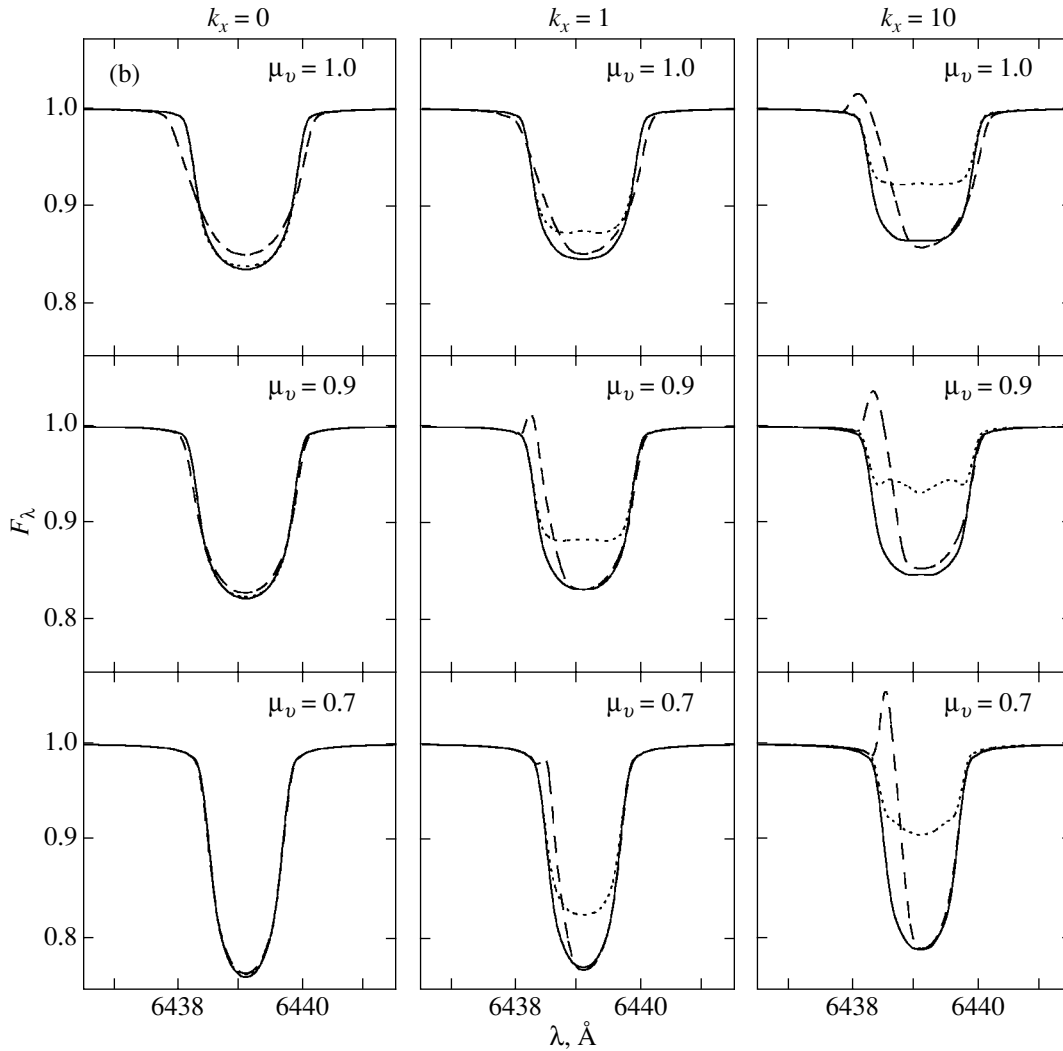


Fig. 5. (Contd.)

star is viewed from the side, since it has its maximum extent along the line connecting the component centers. The X-ray heating results in a more complex temperature distribution over the stellar surface and more complex orbital variability of the line profile due to the formation of the emission component. As a result, if the relative luminosity of the X-ray source is significant, the line profile becomes narrow rather than broader at quadrature.

The line profiles plotted in Fig. 2 show that the behavior of the line is similar for $q = 1$ and $q = 10$, but the depth of the profile increases when q is increased. The emission component of the profile remains fairly prominent when the orbital inclination is decreased from $i = 90^\circ$ (Fig. 2a) to $i = 45^\circ$ (Fig. 2b).

Figures 3–5 show the dependence of the line profiles on the binary parameters q , i , and μ_v and the parameter k_x characterizing the power of the incident X-ray flux.

The dependence of the theoretical profiles on $q = M_x/M_v$ and k_x is shown in Fig. 3. The component-mass ratio was varied from 1 to 20, and the value of k_x from 0 (no X-ray heating) to 50 (very strong X-ray heating). The star completely filled its Roche lobe ($\mu_v = 1$). The orbital inclination was specified to be $i = 90^\circ$ (Fig. 3a) or $i = 45^\circ$ (Fig. 3b). For each set of parameters, the figures show line profiles for three typical orbital phases: $\varphi = 0$ (when the X-ray source is behind the optical star), $\varphi = 0.25$ (quadrature), and $\varphi = 0.5$ (the X-ray source is in front of the optical star). Similarly, Figs. 4 and 5 show line profiles for other sets of system parameters.

The plots in Fig. 3 show that, in the absence of X-ray heating, the width of the absorption profile is nearly the same for different q values, decreasing only very slightly when q is increased from 1 to 20. The increased contribution of the emission component when the X-ray heating is increased from $k_x = 0$ to

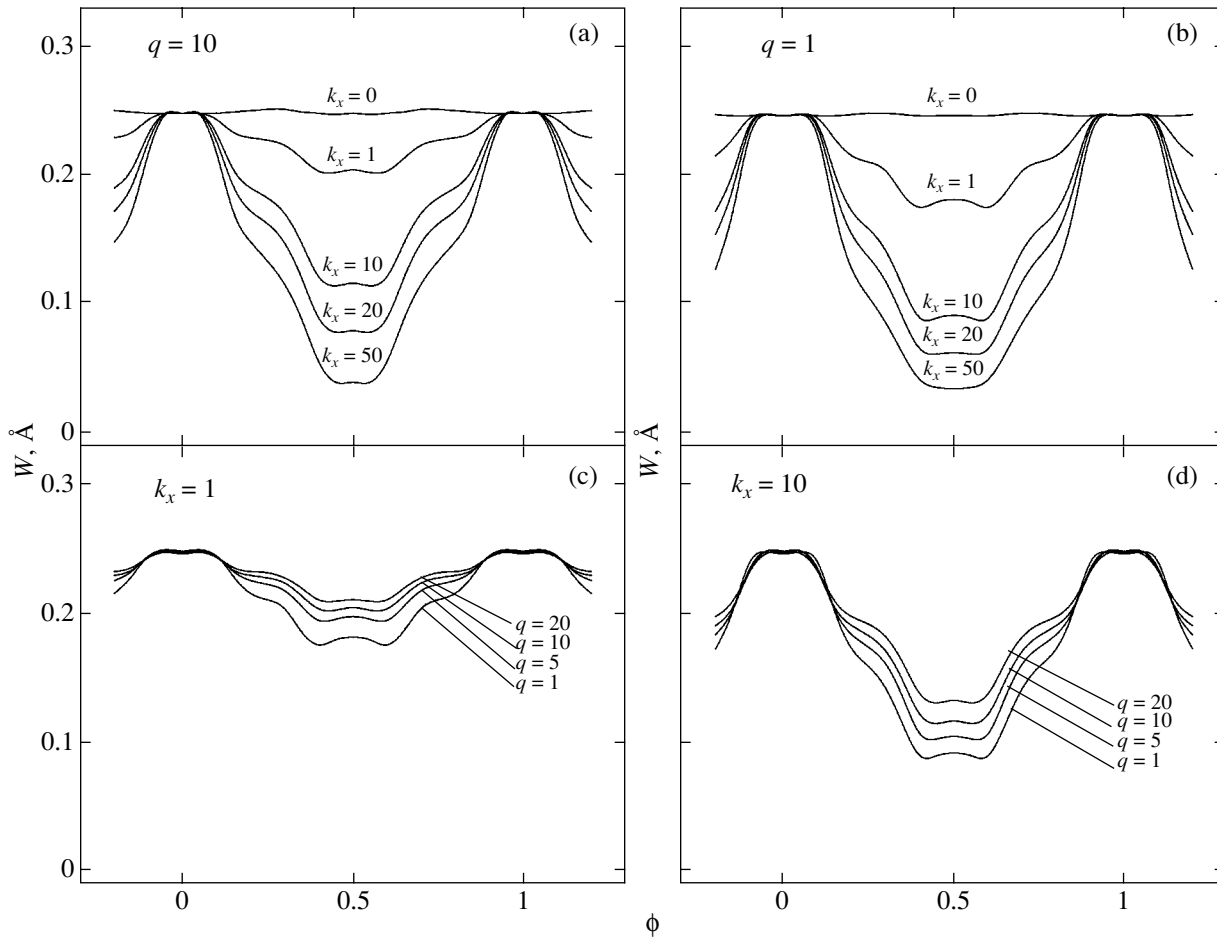


Fig. 6. Orbital-phase variations of the equivalent widths of the Ca I $\lambda 6439$ Å line in the spectrum of the optical star for (a) $k_x = 0-50$, $q = 10$, $\mu_v = 1$, and $i = 90^\circ$; (b) the same but with $q = 1$; (c) $q = M_x/M_v = 1-20$, $k_x = 1$, $\mu_v = 1$, and $i = 90^\circ$; (d) the same but with $k_x = 10$; (e) $\mu_v = 0.7-1$, $k_x = 1$, $q = 10$, and $i = 90^\circ$; (f) the same but with $k_x = 10$; (g) $i = 30^\circ, 60^\circ, 90^\circ$ with $k_x = 1$, $q = 10$, and $\mu_v = 1$; (h) the same but with $k_x = 10$. The temperature of all the models is $T = 5000$ K.

$k_x = 50$ with q constant is clearly visible. The emission component is more prominent for lower q , k_x being the same. This effect is already clearly visible when $k_x = 1$ (compare the profiles for $q = 1$ and $q = 20$); the effect first becomes more pronounced as k_x is increased ($k_x = 10-20$), but then weakens. When the X-ray heating is very strong ($k_x = 50$), the differences between the profiles for different q values are small.

Figure 4 shows the dependence of the line profiles on the power of the X-ray heating ($k_x = 0, 1, 10$) and the orbital inclination ($i = 30^\circ, 60^\circ, 90^\circ$). Computations were carried out for the two component-mass ratios $q = 10$ (Fig. 4a) and $q = 1$ (Fig. 4b). We draw the following main conclusions: (1) the width of the profile increases and the depth decreases with increasing i ; (2) the profiles vary with orbital phase more strongly when i is larger; (3) the emission component of the line profile that forms as the X-ray

heating becomes more powerful is appreciable even at low orbital inclination $i = 30^\circ$; (4) the profiles vary more with orbital phase for $q = 1$ than for $q = 10$, i being the same.

Figure 5 shows the dependence of the line profiles on the size of the star (defined by the Roche-lobe filling coefficient). The rotation of the star is assumed to be synchronous with the orbital motion for both $\mu_v = 1$ and $\mu_v < 1$. Theoretical line profiles are shown for $\mu_v = 0.7, 0.9, 1$ and $k_x = 0, 1, 10$. The data for $i = 90^\circ$ are plotted in Fig. 5a, and those for $i = 45^\circ$ in Fig. 5b. The component-mass ratio was fixed at $q = 10$. We draw the following conclusions: (1) the variability with orbital phase becomes more pronounced when the X-ray heating is increased for all values of μ_v from 0.7 to 1; (2) the profiles become broader when μ_v is increased (due to the increase in the size of the star and, accordingly, the increase in the velocity dispersion at the stellar surface); (3) the

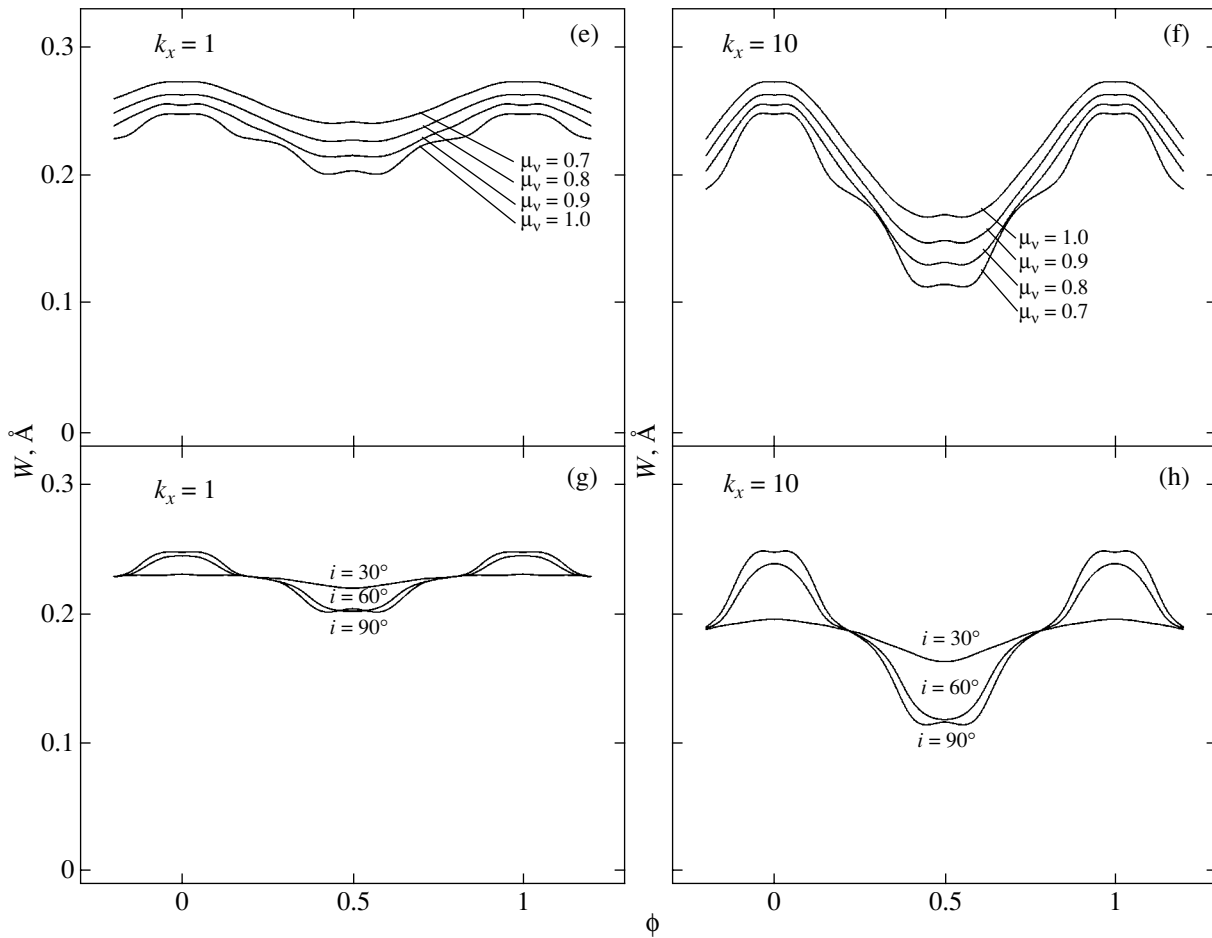


Fig. 6. (Contd.)

intensity of the emission component is higher when the star does not fully fill its Roche lobe. This last effect is due to the relative increase of the fraction of the stellar surface that is heated by the incident X-rays when k_x is constant and μ_v decreases; therefore, the contribution of the heated part of the star to the total radiation increases.

Thus, our modeling of the theoretical CaI $\lambda 6439$ Å line profiles for various parameters of an X-ray binary system leads to the following main conclusions.

(1) X-ray heating of an optical star with temperature $T = 5000$ K gives rise to an emission component in the CaI $\lambda 6439$ Å absorption profile. The line profile varies with orbital phase. The intensity of the emission component is higher and its variability with orbital phase more pronounced in the presence of more powerful X-ray heating.

(2) We obtain the following dependence on q . The value of k_x being the same, the emission component is stronger when q is low if the X-ray heating is weak

or moderate. In the case of very strong X-ray heating, the differences between the profiles for different q values are small.

(3) We obtain the following dependence on i . The intensity of the emission component becomes higher and its variability with orbital phase more pronounced when the orbital inclination i is increased. The emission component is clearly visible even for small inclinations, $i \sim 30^\circ$.

(4) We obtain the following dependence on the Roche-lobe filling coefficient μ_v . The value of k_x being the same, a star that does not fully fill its Roche lobe has a stronger emission component than a star that fills its Roche lobe.

Note that the theoretical CaI $\lambda 6439$ Å line profiles were not corrected for the instrumental profile of the detector. The detection of differences between profiles in real spectrograms requires a dispersion of ~ 0.1 Å per pixel; i.e., a resolution of $R \sim 50000$. Spectra with such resolution for 20^m stars (typical for an X-ray nova in quiescence) can be obtained only using the largest (8–10 m diameter) telescopes. However, the

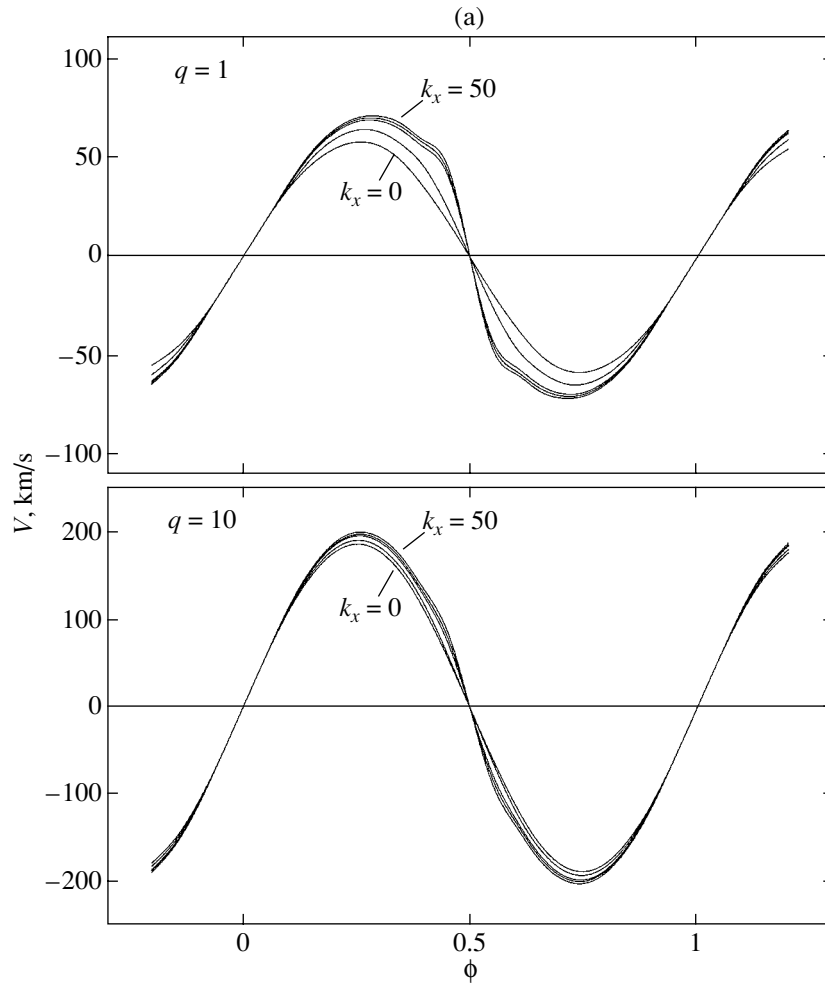


Fig. 7. Dependence of the (a) radial-velocity curves of the optical star and (b) equivalent widths of the CaI $\lambda 6439$ Å line on orbital phase for $k_x = 0, 1, 10, 20, 50$. Data are shown for the two component-mass ratios $q = 1$ and 10. The amplitude of the radial velocity increases with increasing k_x . The model parameters are $q = 10$, $\mu_v = 1$, $T = 5000$ K, $i = 90^\circ$, and $P = 12^d$.

line equivalent widths do not depend on the instrumental profile (only the problem of line blending remains), so the analysis of equivalent widths is possible using lower resolutions of at least $R \sim 10\,000$.

Figure 6 shows the variations of the equivalent width of the CaI $\lambda 6439$ Å line with orbital phase for various parameters of the X-ray system. The equivalent widths were computed for the entire theoretical profile, including the emission component. The variations of the equivalent widths with the power of the X-ray source ($k_x = 0-50$) are plotted for the two component-mass ratios $q = 10$ (Fig. 6a) and $q = 1$ (Fig. 6b). As we already noted above, when q is low, the variability of the line with orbital phase is stronger in the case of weak heating ($k_x = 1$). As k_x is increased, this effect becomes less pronounced, and the orbital variability of the profile is virtually identical for low and high q when the heating is very strong ($k_x = 50$).

The variations of the equivalent widths with the component-mass ratio (for $q = 1-20$) are shown for weak ($k_x = 1$) and strong ($k_x = 10$) X-ray heating in Figs. 6c and 6d, respectively. The orbital variability substantially increases in the case of strong heating, and is also higher for lower q .

The differences between the line equivalent widths for different Roche-lobe filling factors μ_v are shown in Fig. 6e for $k_x = 1$ and Fig. 6f for $k_x = 10$. The equivalent widths are larger for smaller μ_v , but the μ_v dependence of the amplitude of their variability relative to the values at phase 0 is weaker.

The dependences of the variability of the line equivalent widths on the orbital inclination ($i = 30^\circ-90^\circ$) are shown in Fig. 6g ($k_x = 1$) and Fig. 6h ($k_x = 10$). Variability is present for $i = 30^\circ$, and becomes substantially stronger with increasing i .

The radial-velocity curves as functions of the X-ray heating power k_x are shown in Fig. 7a (for

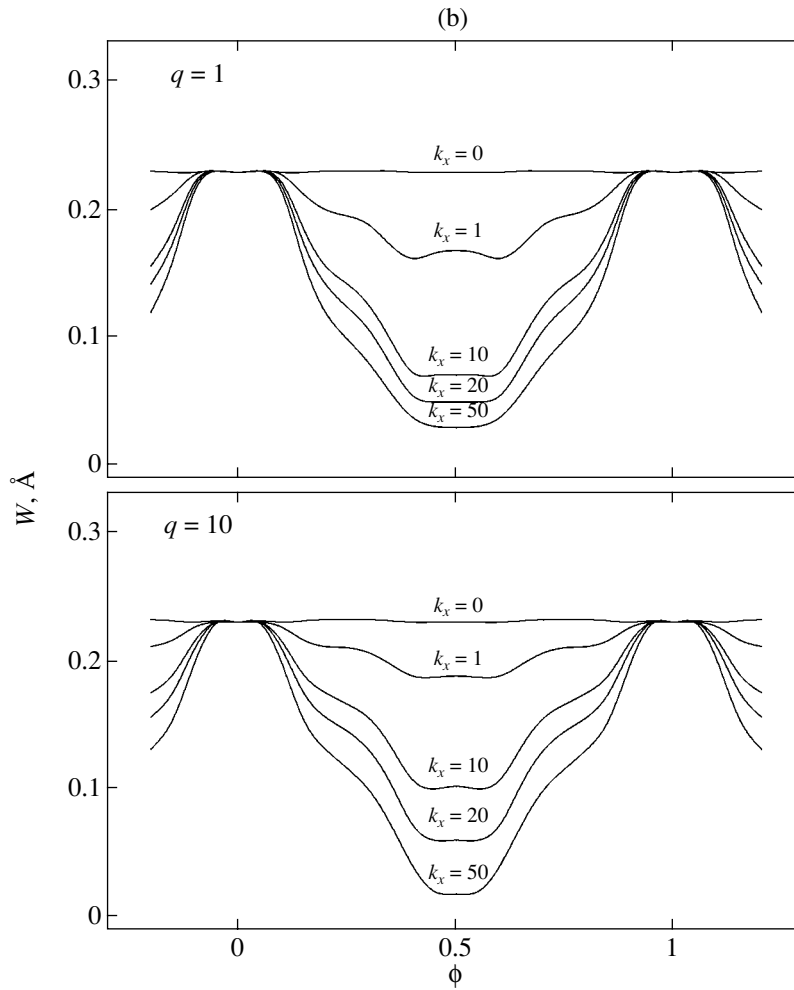


Fig. 7. (Contd.)

$q = 1$ in the upper panel and $q = 10$ in the lower panel). The curves were computed for the CaI $\lambda 6439.075 \text{ \AA}$ line. Figure 7b shows the corresponding variations of the line equivalent widths with orbital phase. The radial velocities were derived as is described in [4] (using three levels: one-third, one-half, and two-thirds of the depth at the line center). The amplitude of the radial velocity grows with k_x , with this effect being more pronounced for $q = 1$ than for $q = 10$.

The growth of the radial-velocity amplitude with k_x is related to the formation of the emission component in the profile. Emission arises in surface elements on the heated side of the star; i.e., in the region with lower radial velocities. Effectively, the absorption profile narrows and the apparent radial velocity increases. The effect is more pronounced for low q (lower masses of the relativistic companion), since the distance between the relativistic object and the surface of the optical star is then lower, so that

a relatively larger fraction of the emitted X-ray flux irradiates the surface of the optical star.

Figure 8 shows a three-dimensional plot of the wavelength and orbital-phase dependence of the intensity in the line profile for $k_x = 10$ and $q = 10$. Half of the orbital period is shown. A comparison of this theoretical dependence with the corresponding observed three-dimensional dependence can be used to determine the most important parameters of a close binary: the component masses and orbital inclination.

5. CONCLUSION

Our method for computing absorption-line profiles for X-ray systems, taking into account heating of the stellar atmosphere by external radiation, can be applied to detailed analyses of high-resolution spectra of X-ray binaries. This provides additional opportunities for the reliable estimation of the physical parameters of X-ray binaries, first and foremost, the

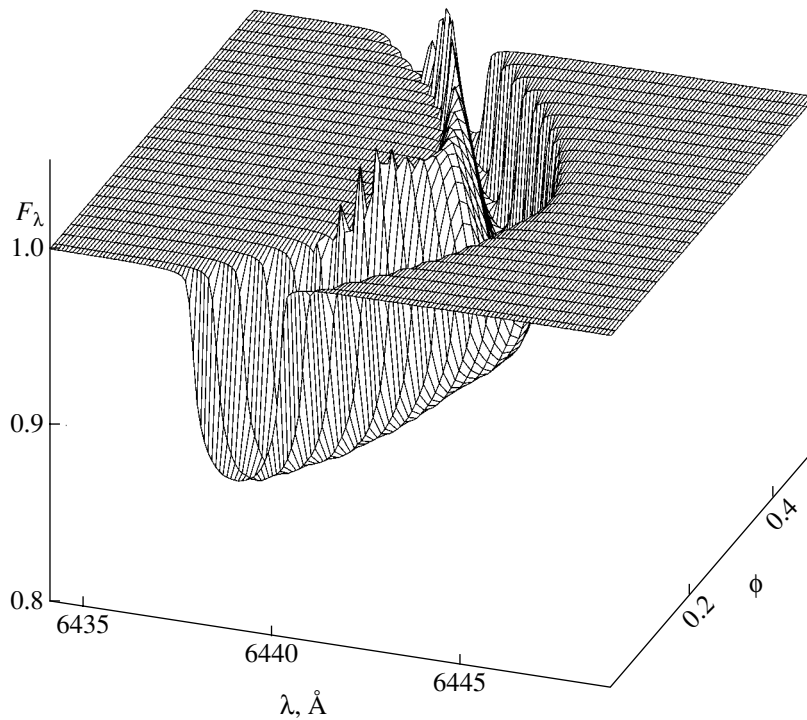


Fig. 8. Three-dimensional dependence of the distribution of the intensity in the Ca I $\lambda 6439$ Å profile on wavelength and orbital phase for $k_x = 10$, $M_v = 1M_\odot$, $M_x = 10M_\odot$, $\mu_v = 1$, $T = 5000$ K, and $i = 90^\circ$.

masses of neutron stars and black holes in such binaries. The realization of these possibilities requires high-resolution ($R \approx 50\,000$) optical spectra of X-ray binaries using modern, large, new-generation telescopes. We hope that applying our method to the interpretation of such spectra will make it possible to obtain more precise estimates of the masses of relativistic objects and reduce the errors in these masses. This is important for verifying the existence of a bimodal distribution for the masses of neutron stars and black holes [31], which is important both for our understanding of the late stages of the evolution of massive stars and the physics of the core collapse in such stars and for testing modern theories of gravitation [32].

ACKNOWLEDGMENTS

This work was supported by the Russian Foundation for Basic Research (project nos. 02-02-17524 and 02-02-17174) and the Program of Support for Leading Scientific Schools of Russia (grants NSh-388.2003.2, and NSh-1789.2003.2). E.A.A. is grateful to Prof. G. Brown for providing the possibility to use computer facilities at Glasgow University (United Kingdom).

REFERENCES

1. E. A. Antokhina and A. M. Cherepashchuk, *Pis'ma Astron. Zh.* **23**, 889 (1997) [*Astron. Lett.* **23**, 773 (1997)].
2. T. Shahbaz, *Mon. Not. R. Astron. Soc.* **298**, 153 (1998).
3. M. K. Abubekero, E. A. Antokhina, and A. M. Cherepashchuk, *Astron. Zh.* **81**, 606 (2004) [*Astron. Rep.* **48**, 550 (2004)].
4. E. A. Antokhina and A. M. Cherepashchuk, *Astron. Zh.* **71**, 420 (1994) [*Astron. Rep.* **38**, 367 (1994)].
5. E. A. Antokhina, *Astron. Zh.* **73**, 532 (1996) [*Astron. Rep.* **40**, 483 (1996)].
6. R. L. Kurucz, *Astrophys. J., Suppl. Ser.* **40**, 1 (1979).
7. E. A. Antokhina, A. M. Cherepashchuk, and V. V. Shimanskii, *Izv. Akad. Nauk, Ser. Fiz.* **67**, 293 (2003).
8. R. E. Wilson, *Astrophys. J.* **234**, 1034 (1979).
9. H. Von. Zeipel, *Mon. Not. R. Astron. Soc.* **84**, 684 (1924).
10. L. B. Lucy, *Z. Astrophys.* **65**, 89 (1967).
11. R. L. Kurucz, SAO CD-ROMs, Cambridge, MA02138, USA (1994).
12. N. A. Sakhbullin and V. V. Shimanskii, *Astron. Zh.* **73**, 73 (1996) [*Astron. Rep.* **40**, 62 (1996)].
13. M. Milgrom, *Astrophys. J.* **206**, 869 (1976).
14. N. A. Sakhbullin and V. V. Shimanskii, *Astron. Zh.* **73**, 793 (1996) [*Astron. Rep.* **40**, 723 (1996)].
15. D. G. Yakovlev, L. M. Band, M. B. Trzhaskovskaya, *et al.*, *Astron. Astrophys.* **237**, 267 (1990).

16. D. V. Ivanova, N. A. Sakhbullin, and V. V. Shimanskii, *Astron. Zh.* **79**, 433 (2002)[*Astron. Rep.* **46**, 390 (2002)].
17. V. F. Suleimanov, *Pis'ma Astron. Zh.* **22**, 107 (1996) [*Astron. Lett.* **22**, 92 (1996)].
18. R. L. Kurucz, *SAO Spec. Rep.* **309**, 1 (1970).
19. V. F. Suleymanov, *Astron. Astrophys. Trans.* **2**, 197 (1992).
20. N. A. Sakhbullin and V. V. Shimanskii, *Astron. Zh.* **74**, 432 (1997)[*Astron. Rep.* **41**, 378 (1997)].
21. S. E. Nersisyan, A. V. Shavrina, and A. A. Yaremchuk, *Astrofizika* **30**, 247 (1989)[*Astrophys.* **30**, 247 (1989)].
22. H. R. Griem, *Astrophys. J.* **132**, 883 (1960).
23. M. J. Seaton, C. J. Zeippen, J. A. Tully, *et al.*, *Rev. Mex. Astron. Astrofis.* **23**, 19 (1992).
24. A. A. Radtsig and B. M. Smirnov, *Atom and Atom Ions Parameters* (Énergoatomizdat, Moscow, 1986) [in Russian].
25. A. J. Barnard, J. Cooper, and L. J. Shamey, *Astron. Astrophys.* **1**, 28 (1969).
26. D. Mihalas, A. J. Barnard, J. Cooper, *et al.*, *Astrophys. J.* **190**, 315 (1974).
27. A. Unsold, *Physik der Sternatmosphären* (Springer, Berlin—Göttingen—Heidelberg, 1955).
28. R. L. Kurucz and I. Furenlid, *Sample Spectral Atlas for Sirius*. *SAO Spec. Rep.* **387**, 1 (1979).
29. E. Anders and N. Grevesse, *Geochim. Cosmochim. Acta* **53**, 197 (1989).
30. D. V. Ivanova, N. A. Sakhbullin, and V. V. Shimanskii, *Astron. Zh.* **81**, 523 (2004).
31. A. M. Cherepashchuk, *Usp. Fiz. Nauk* **173**, 345 (2003)[*Phys. Usp.* **46**, 325 (2003)].
32. K. A. Postnov and A. M. Cherepashchuk, *Astron. Zh.* **80**, 1075 (2003)[*Astron. Rep.* **47**, 989 (2003)].

Translated by L. Yungel'son